Engineering 59 (2026) 256–270

Contents lists available at ScienceDirect

Engineering

journal homepage: www.elsevier.com/locate/eng

Research
Low Carbon Transformation for Conventional Energies—Article

Developing Flue Gas-Driven Molten-Salt-Heat-Exchanger for Flexible Operation of Coal-Fired Power Plant

Jinliang Xu [a,b,c,*], Hongliang Su [a,b,d], Xinyu Dong [a,b], Xiongjiang Yu [a,b], Chao Liu [b], Yan Wang [b], Jian Xie [a,c], Wei Wang [b], Yupu Yu [b], Qinghua Wang [b], Yuguang Niu [b], Jizhen Liu [b], Ying Huang [d], Zhengshun Zhang [d], Anyou Dong [b], Yan Pan [b], Hao Wu [b]

[a] Beijing Key Laboratory of Multiphase Flow and Heat Transfer for Low Grade Energy Utilization, North China Electric Power University, Beijing 102206, China
[b] Beijing Huairou Laboratory, Beijing 101400, China
[c] Key Laboratory of Power Station Energy Transfer Conversion and System (North China Electric Power University), Ministry of Education, Beijing 102206, China
[d] Harbin Boiler Company Limited, Harbin 150046, China

ARTICLE INFO

Article history:
Received 8 February 2025
Revised 28 August 2025
Accepted 2 September 2025
Available online 6 September 2025

Keywords:
Heat storage
Molten-salt-heat-exchanger
Heat transfer coefficient
Flexibility
Coal-fired power plant

ABSTRACT

The large-scale utilization of renewable energy challenges the stability and safety of the grid; thus, the flexibility of coal-fired power plants should be increased to balance unstable renewable energies. To achieve this, a heat storage system (HSS) is integrated into a power plant. This is the first study utilizing furnace flue gas to drive a molten-salt-heat-exchanger (MSHE). Compared to steam-vapor-driven MSHE, flue gas-driven technology avoids the pinch temperature limitation (PTL) and simplifies the system configuration. In this study, we demonstrate the concept, design, fabrication, and experiments of the MSHE. The novelties include: ① finned tubes to balance the thermal resistances between the flue gas side and the molten salt side; ② a weak angle design to ensure gravity-driven recession of the molten salt; and ③ a modular design to ensure even temperature distribution at the outlet of the tube bundles. A heat transfer correlation is developed for molten salt, covering a wide range of Reynolds numbers. An experimental setup is constructed to collect data and verify the effectiveness of the MSHE. The measured overall heat transfer coefficients matched the predictions well, with deviations of less than 10%. The measured heat power reached 320 kW, exceeding the 300 kW design target. We demonstrate the heat transfer between the flue gas and molten salt to compensate for the heat release from the HSS to the environment, reducing electricity consumption in the standby stage of the system. The modular design of the MSHE ensures minimal temperature deviations of < 4 K among different tubes, avoiding local overheating-induced decomposition of the molten salt. Based on the 300 kW MSHE results, a 10 MW MSHE is designed, fabricated, and integrated into a 350 megawatt electric (MWe) coal-fired plant to achieve a higher load variation rate of 6% Pe·min^{-1} for a coal-fired power plant.

© 2025 THE AUTHORS. Published by Elsevier LTD on behalf of Chinese Academy of Engineering and Higher Education Press Limited Company. This is an open access article under the CC BY-NC-ND license (http://creativecommons.org/licenses/by-nc-nd/4.0/).

1. Introduction

Developing a sustainable, low-carbon economy is a global priority [1]. To achieve this target, large-scale utilization of renewable energy sources, such as solar and wind, is necessary [2]. The European Union (EU) expects massive utilization of renewable energy combined with smart grids and sustainable economic activities such as housing, transport, and industry [3]. Other countries, such as China, the United States, and Australia, perform similar activities [4]. In China, the installed power capacity of nonfossil fuels accounted for more than 50% of the total installed power capacity by 2023 [5]. A recent report from the International Energy Agency Clean Coal Center commented on the growing capacity of renewable energy plants worldwide and the effects of their intermittent and highly variable outputs on the operation of coal-fired plants [6]. Theoretically, intermittent and unstable renewable energies can be compensated for by energy storage on a multiscale timescale from seconds to hours. Unfortunately, no energy storage systems can supply a large capacity to fill this gap on the grid side

* Corresponding author.
E-mail address: xjl@ncepu.edu.cn (J. Xu).

https://doi.org/10.1016/j.eng.2025.09.001
2095-8099/© 2025 THE AUTHORS. Published by Elsevier LTD on behalf of Chinese Academy of Engineering and Higher Education Press Limited Company.
This is an open access article under the CC BY-NC-ND license (http://creativecommons.org/licenses/by-nc-nd/4.0/).

[7]. Therefore, gas- or coal-fired power plants should switch their roles from basic (electric) load suppliers to adjustable energy sources to balance the unstable energy [8].

Several index parameters, including load variation speed, frequency regulation, and startup and shutdown times, characterize the flexibility of coal-fired power plants. Gas turbine systems quickly respond to grid demand, with a load variation speed of (5%–8%) Pe·min^{-1} [9], but coal-fired systems have a slower response, with a load variation speed of 2% Pe·min^{-1} [10]. Further increases in flexibility cause serious safety issues [10], including fray-out-of-flame under ultra-low load operation, damage to cooling wall tubes due to a mismatch between the furnace side and tube side, thermal stress-induced deformation of components, and fatigue damage of thick-wall pressure vessels.

Numerical simulations have shown that the addition of a heat storage system (HSS) to a thermal plant is a potential approach to sustaining power grid stability [11]. Various methods have been proposed for improving the performance of thermal power plants [12–14]. The integration of hot water tanks into a 200 MW power plant has demonstrated a 21.96 MW reduction in the minimum power load [15]. Using the developed simulation models, the integration of a steam accumulator into a thermal power plant is expected to increase the flexibility of the system, indicating that charging a thermal energy system reduces the minimum power load by as much as 7% [16].

To increase the load variation speed for current applications, an additional HSS is integrated into thermal power plants to decouple the thermal connection between the boiler and turbine (Fig. 1). When a portion of the heat generated by the boiler is stored in the HSS, the steam flow rate entering the turbine decreases, reducing the power output. Conversely, when the HSS discharges heat to generate additional steam entering the turbine, the turbine output increases.

As molten salt has been successfully applied in solar thermal plants [17], it is currently used as a working fluid for thermal energy storage. The coupling of the boiler and HSS is an important issue. Various investigations have been conducted to extract steam vapor from thermal power plants to heat the molten salt [18]. Currently, several projects are being conducted in China to extract steam vapor for heat storage. The disadvantages of steam extraction technology are summarized as follows: ① Under low load ratios, the thermal plant operates at subcritical pressure, and the superheated vapor extracted from the thermal system loses its heat to the molten salt through three heat transfer stages: a superheated vapor section, a condensation section, and a subcooled water section (Fig. 2). Consequently, three heat exchangers are required, increasing the complexity and cost of the HSS. ② The three-stage heat transfer creates a pinch temperature limitation (PTL), which restricts the increase in molten salt temperature and, in turn, minimizes the generated vapor temperature during the heat discharge process (Fig. 2(a)). The pinch temperature is the minimal temperature difference that characterizes the uniformity of the temperature gradient along the heat transfer pathway [19], depending on the fluid states on either side of the heat exchanger. A better thermal match occurs when the fluid states on both sides are similar, resulting in the absence of a PTL. However, if the fluid states differ, such as a liquid state on the cold side and a combination of single-phase (gas or liquid) and two-phase mixtures on the hot side, a poorer thermal match occurs, generating the PTL and limiting the temperature rise on the cold side (Fig. 2). ③ If a higher molten salt temperature is desired, only part of the steam energy extracted from the boiler can be absorbed by the molten salt, thereby reducing the heat storage efficiency (Fig. 2(b)).

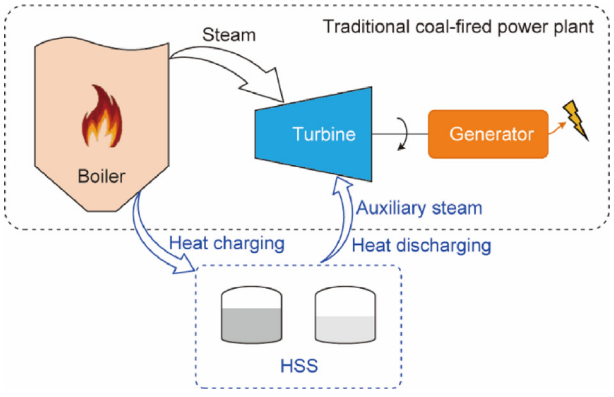

Fig. 1. Concept of the heat storage system integrated with a coal-fired power plant.

To overcome these shortcomings, we propose a direct flue gas heating technology to drive a molten-salt-heat-exchanger (MSHE). Because a phase change does not occur during the heat transfer between the flue gas and molten salt, PTL does not exist. Thus, only a single heat exchanger is required, which simplifies the system configuration and reduced the HSS cost. It should also be noted that steam is a high-grade energy source. The steam extraction technique reduces the round-trip efficiency. Alternatively, the direct flue gas heating technique increases round-trip efficiency. To the best of our knowledge, an experimental investigation of flue gas-driven MSHE has not been reported in the literature. The remainder of this paper is organized as follows: Section 2 describes the experiments and methods, including the challenges of MSHE, concept design and fabrication of MSHE, and the data reduction process. Section 3 presents and discusses the results. Section 4 discusses the engineering applications of the MSHE. The conclusions are summarized in Section 5.

2. Experiments and methods

Before presenting the experiments and methods, we discuss the challenges of the MSHE.

2.1. Challenges of the MSHE

Several issues must be addressed to develop flue-gas-heating technologies. First, the extracted flue gas must have a reasonable temperature range. Temperatures that are too high may cause decomposition of the molten salt, threatening its safety of the molten salt. However, an excessively low temperature decreases the temperature difference between the flue gas and molten salt. Thus, we extract the flue gas in the medium temperature level covering a range of 450–650 °C. Second, what is the maximum flow rate of flue gas that can be extracted from the furnace? The flue gas extraction clearly disturbs the thermal balance between the various components of the boiler. Once part of the flue gas is extracted from the furnace, the steam temperature and flow rate of the boiler components, such as the reheater and superheater, can be changed. Therefore, the quantity of flue gas must be refined. Our numerical simulation showed that, if the extracted flow rate of the flue gas was less than 35% of the total value, the effect of flue gas extraction on the boiler was acceptable. Correspondingly, the extracted heat power reached 5% of the total thermal load of the furnace. For a 350 megawatt electric (MWe) coal-fired power plant, 10 MW of heat power can be absorbed by the HSS. Third, after releasing flue gas energy into the molten salt, where does the flue gas return to the furnace? Here, we assign the flue gas temperature to be ~300 °C at the MSHE outlet. The "colder" stream of flue gas can return to the furnace at the selective catalytic reduction (SCR) inlet.

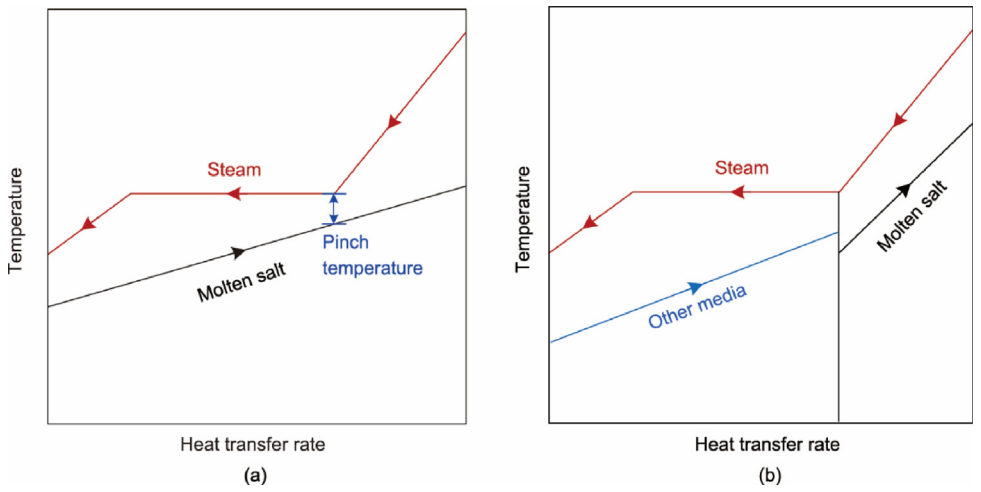

Fig. 2. The heat transfer roadmaps for the steam extraction heat storage method. (a) The pinch temperature limit (PTL) restricts the molten salt temperature rise; (b) only a portion of the flue gas energy is absorbed by the molten salt.

Notably, the above issues are discussed at the system level. In contrast to the system level, the MSHE component is focused on the MSHE components.

Mismatch of thermal resistances. For the MSHE, the heat transfer coefficients are larger for the convection heat transfer of molten salt than those of flue gas. The mismatch of thermal resistances between the molten salt and flue gas is serious, guiding us to enhance the heat transfer on the flue gas side. Without heat transfer enhancement, the MSHE should be ultralarge, which is not acceptable for practical applications.

Solidification and decomposition of molten salt. For HSS, the liquid state of the molten salt should be ensured. Overheating the molten salt causes decomposition, which changes its chemical composition and physical properties. However, once the molten salt reaches the solidification temperature, it begins to solidify, blocking the pipeline or vessel. Experience has been gained from solar thermal plants to prevent salt from solidifying [20,21]. Electric wires warm the molten salt to maintain its temperature above its solidification point [22,23]. Electric heating is difficult to perform in MSHE applications. To overcome the solidification challenge, the HSS operation and MSHE design should be considered. From an operational perspective, a suitable temperature range for flue gas should be chosen, as has already been mentioned. Importantly, the MSHE should be designed such that the stored salt can be automatically vacuumed from the tubes before turning off the system.

Deposited-ash-particles-layer induced thermal resistance. The flue gas contains solid ash particles, which may deposit on the heat exchanger surface and deteriorate heat transfer. The convective flushing of flue gas in heat transfer tubes may also spoil these tubes. Hence, a gas–solid separator separates solid particles from the flue gas, collecting solid particles larger than 10 μm. Usually, an ultrasonic ash blower is used for the periodic operation of the HSS.

2.2. Design and fabrication of the MSHE

An MSHE conceptual design was proposed to address these challenges (Fig. 3). An MSHE with a rated power of 300 kW was designed, fabricated, and tested. The MSHE was driven by a 10 MW thermal load furnace. A rated power of 300 kW corresponds to the rated inlet temperature of flue gas $T_{fg,in}$ = 650 °C, volume flow rate of flue gas m_{fg} = 3500 $Nm^3 \cdot h^{-1}$, inlet temperature of molten salt $T_{s,in}$ = 320 °C, and volume flow rate of molten salt m_s = 1.7 $m^3 \cdot h^{-1}$. The expected temperature of the molten salt is 550 °C after being heated by flue gas. Chinese Shenghua bituminous coal was used as fuel. The flue gas contained powdered dust with a concentration of approximately 24 $g \cdot Nm^{-3}$. The flue gas had volume concentrations of 74.75% N_2, 7.71% CO_2, 0.07% SO_2, 6.41% water vapor, and 11.09% O_2. The physical properties of the flue gas were calculated based on the concentrations of various species at different operating temperatures. The heat storage capacity is given by $Q_{fg} = m_{fg} c_{p,fg} (T_{fg,in} - T_{fg,out})$, where $c_{p,fg}$ is the specific heat of the flue gas, $T_{fg,in}$ and $T_{fg,out}$ are the temperatures of the flue gas entering and leaving the MSHE, respectively. At a normal operating load of 5 MW for the furnace, assuming a maximum of 70% of the total flue gas for m_{fg}, $T_{fg,in}$ = 650 °C and $T_{fg,out}$ = 450 °C, Q_{fg} was evaluated as 349 kW to achieve a 300 kW capacity for the design target.

A binary nitric acid-based molten salt, also called solar salt, is used as the working medium for heat storage and contains mass concentrations of ~60% $NaNO_3$ and ~40% KNO_3. The melting and decomposition temperatures of the molten salt were 220 and 585 °C, respectively. This salt is a stable chemical species that operates at high temperatures and has been widely used in solar power plants [24]. The physical properties of the salts were obtained from the literature [25].

Finned tubes to balance thermal resistances. Finned tubes are used to enhance convection heat transfer on the flue gas side. The fins were welded to the outer walls of the heat transfer tubes. Thus, contact thermal resistance does not exist between the fins and tubes. Because H-type fins are widely applied in industry [26], they were adopted in this study (Fig. 3).

Weak inclination angle for salt receding. The MSHE will have a temperature below the solidification point during the shutdown stage, leading to solidification of the molten salt in the tubes. To avoid this blocking phenomenon, the MSHE should be designed to ensure automatic gravity-driven recession of salt from the tubes. To achieve this target, a 3° inclination angle is set for the tubes with respect to the horizontal axis (Fig. 3). Six rows of snake-shaped heat transfer tubes were used in the demonstrated MSHE prototype. The total flow rate of the salt was distributed into each heat-transfer tube via the corresponding common plenum.

Modular design of the MSHE. For practical operation of the MSHE, the flow and temperature fields may be non-uniform over the cross section of the chimney. The global effect in the height direction may induce a nonuniform temperature distribution of

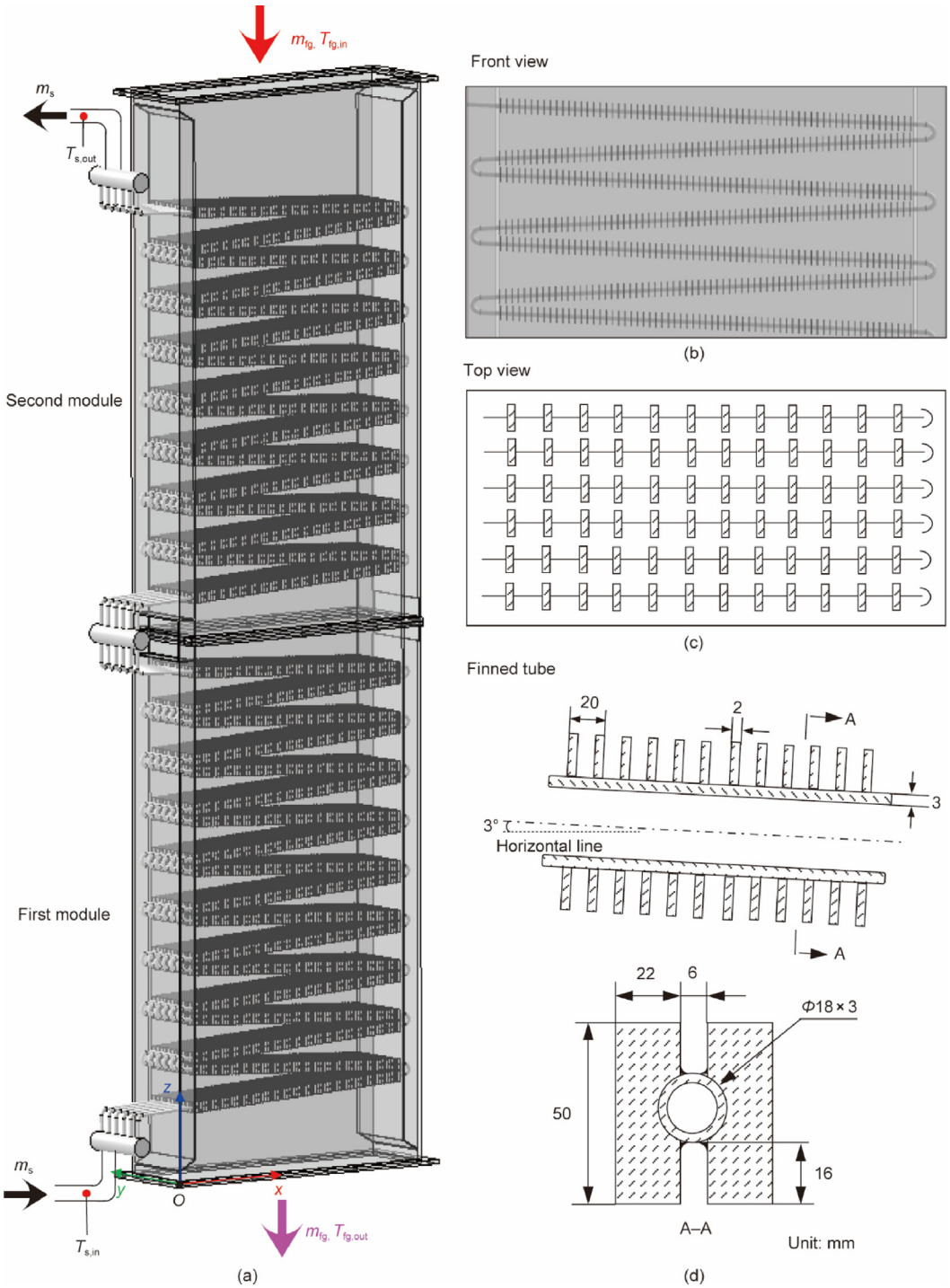

Fig. 3. Design of the MSHE. (a) Three-dimensional drawing of the MSHE; (b) front view of the MSHE; (c) top view of the MSHE; (d) the finned tube and geometry dimensions.

the molten salt in the branch tubes. The salt temperatures were higher than the design value in some tubes, but lower than the design value in others. Overheating salt can cause its decomposition. To eliminate the overheating effect, a modular design was introduced to separate the entire heat exchanger into two modules along the height direction. In the modular design, mixing occurs in the common plenum at the junction of the two modules, and the mixed salt reenters the second module to lower the nonuniform temperature distribution. Another benefit is the enhancement of the convective heat transfer of the molten salt in the second module owing to the thermal boundary layer redevelopment mechanism, which has been verified in previous studies [27].

Figs. 3 and 4(a) show the 3D design and the fabricated module, respectively. The MSHE has the following 3D dimensions 1400 mm × 380 mm × 4955 mm. The heat transfer tube measures Φ18.0 × 3.0 mm with a length of 1200 mm. Each fin has a planar size of 50 mm × 22 mm and a thickness of 2.0 mm, with a 6.0 mm slot to form the "H" shape. For the fin gap, a tradeoff exists between heat transfer enhancement and ash particle deposition on the heat transfer tubes. A sparse fin arrangement weakens heat

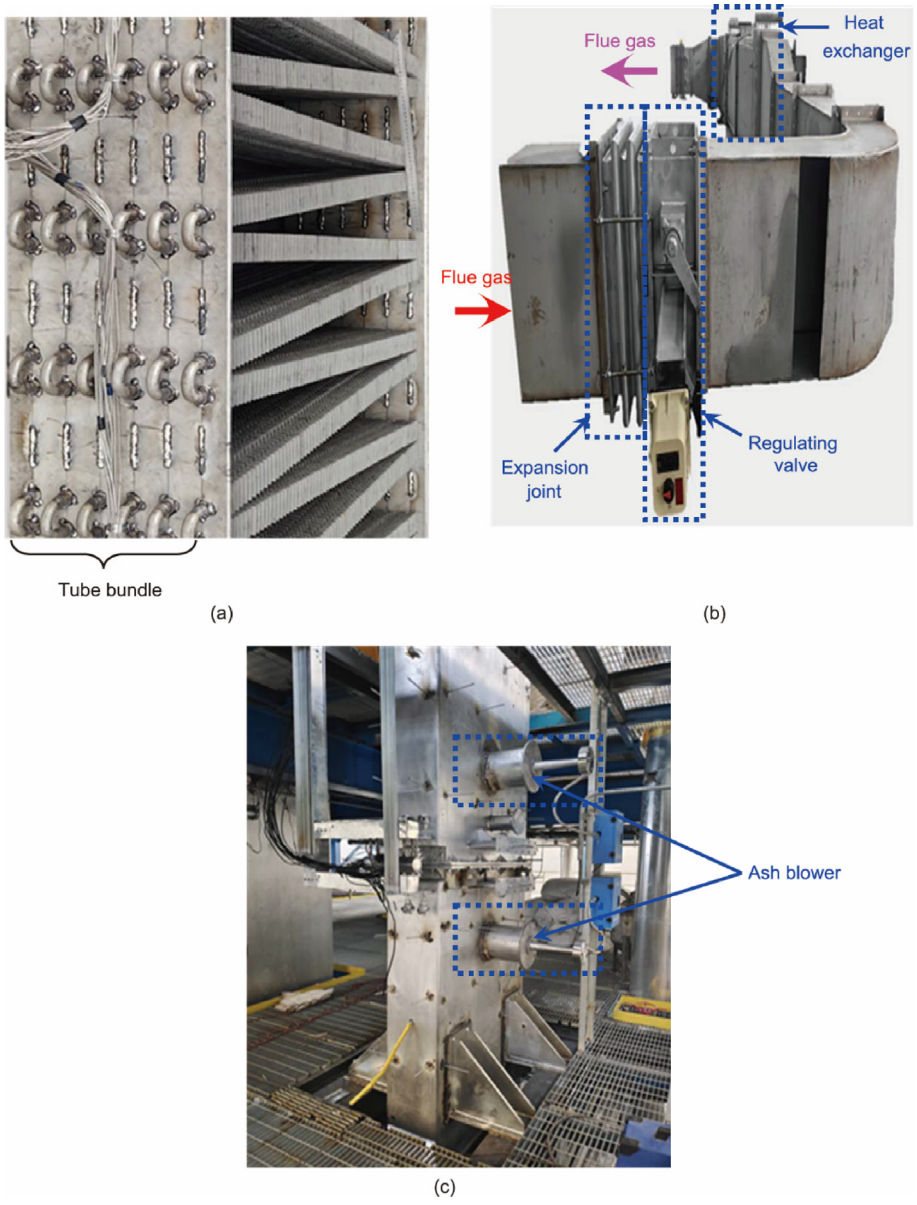

Fig. 4. Photos of the experimental setup. (a) The MSHE prototype; (b) the assembly of the flue gas-driven HSS; (c) the vertically positioned flue gas-driven HSS.

transfer enhancement, whereas a dense fin arrangement promotes ash particle deposition. The fin gap is optimized to 18.0 mm. Since TP347H is commercially used in solar thermal plants [28], it is selected as the base material for the heat transfer tubes. The fin material is S30408 stainless steel. MSHE fabrication is accomplished by welding the fins onto the base tubes. After fabrication, nondestructive testing was conducted to verify the welding quality. A hydrostatic test was performed to ensure the MSHE can withstand ~1.5 MPa without leakage. A compressed air-driven ball-passing test ensures the ball moves freely within the tubes and that the tube surfaces are clean. Fig. 4(b) shows a photo of the horizontally positioned integrated flue gas tunnel. The tunnel primarily integrates an expansion joint, a regulating valve, the MSHE, and related flanges that connect the various elements. The expansion joint compensates for thermal stress-induced deformation of the integrated flue gas tunnel during operation. The regulating valve adjusts the flow rate for flushing the MSHE. Fig. 4(c) shows a photo of the vertical section of the flue gas tunnel integrated with the 10 MW furnace. Two ash blowers are indicated in Fig. 4(c), which are used to clean ash particles from the heat transfer tubes.

2.3. Experiment setup and data reduction

The experimental setup consisted of a 10 MW furnace, a T-junction tunnel, and two tanks containing molten salt (Fig. 5). The experimental setup contained a furnace-driven flue gas loop and a pump-driven molten salt loop, which were coupled via the MSHE. For the flue gas loop, fine coal and air streams were mixed and burned in a furnace to produce high-temperature flue gas. The flame temperature was controlled by the excess air coefficient and cooling intensity at the furnace wall. The flue gas stream was separated into two parts: one part flowed in the main flue gas pipeline, and the other part entered the MSHE tunnel and returned to the main flue gas pipeline. Flue gas valves 4, 5, and 8 assigned the distribution of the flow rate to the main and branch tunnels, respectively. The flow rate of the flue gas in the branch tunnel (m_{fg}) was measured using an ultrasonic flowmeter 10 (SICK, FLOW-SIC100PH) with an uncertainty of 5%. The pressure drop across the MSHE (ΔP_{fg}) was measured using a pressure-drop transducer (ROSEMOUNT, 3051) with an uncertainty of 5%. Flue gas temperatures $T_{fg,in}$ at the MSHE inlet and $T_{fg,out}$ at the MSHE outlet, are

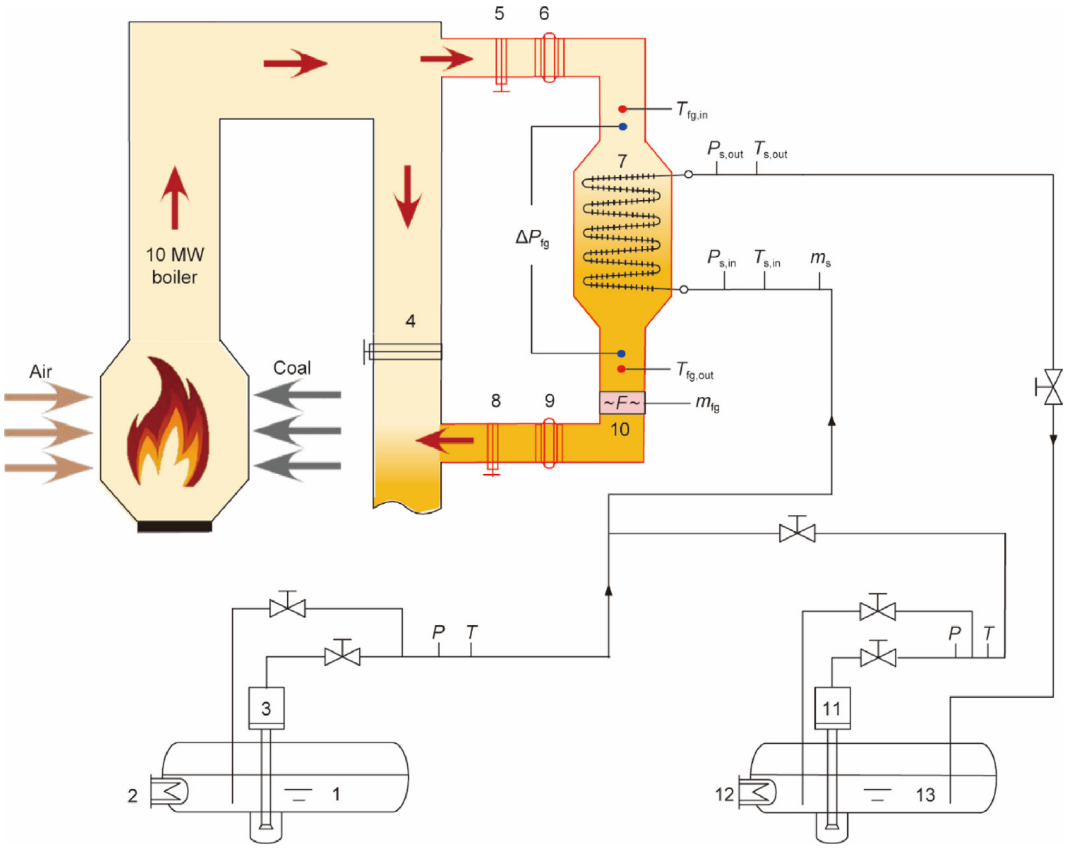

Fig. 5. Experimental setup for the flue gas-driven HSS. 1: cold salt tank; 2 and 12: electric heaters; 3: cold salt pump; 4, 5, and 8: flue gas valves; 6 and 9: expansion joints; 7: MSHE; 10: flue gas flowmeter; 11: hot salt pump; 13: hot salt tank.

measured by the K-type jacket thermocouples with uncertainties of 1 °C.

Attention should be paid to the operation of the molten salt loop, including the heat storage, heat compensation, and salt-receded modes. In the heat storage mode, salt is pumped from the cold tank to be heated by the MSHE and then returned to the hot tank. Once the salt temperature in the hot tank is below the rated value, the heat compensation mode increases the salt temperature in the hot tank, thereby reducing the operating cost by reducing electricity consumption. In contrast to sucking the salt from the cold tank in the heat storage mode, the heat compensation mode pumps the salt from the hot tank to be heated by the MSHE and returns it to the hot tank. Once the salt temperature in the cold tank was below the rated value, the salt was pumped from the hot tank to the cold tank to increase the salt temperature because of the mixing of the two salt streams. The salt-receding mode refers to evacuating all the salt from the system before the HSS is turned off, preventing the salt from solidifying in pipes and vessels. In this study, the rated temperatures were set to 320 °C for the cold tank and 550 °C for the hot tank. Switching of the operation modes can be achieved by running different salt pumps and switching the closed/open state for the related valves. For the molten salt, the temperature is measured by the K-type thermocouple with an uncertainty of 1 °C. The pressure and pressure drop were measured using transducers (ROSEMOUNT, 3051 + 1199) with uncertainties of 1.13%. The flow rate was measured using an ultrasonic flowmeter (OPTISONIC, 4400HT) with an uncertainty of 1%. All the parameters were recorded using a computer-controlled distributed control system (DCS) data collection system.

By measuring m_s, $T_{s,in}$, $T_{s,out}$, m_{fg}, $T_{fg,in}$, and $T_{fg,out}$ (Fig. 5), the heat transfer rate based on the salt side is:

$$Q_s = m_s c_{p,s}\left(T_{s,out} - T_{s,in}\right) \tag{1}$$

The heat transfer rate based on the flue gas side is

$$Q_{fg} = m_{fg} c_{p,fg}\left(T_{fg,in} - T_{fg,out}\right) \tag{2}$$

Thus, the heat transfer efficiency is $\eta = Q_s/Q_{fg}$, which is in the range of 0.95–0.99 in the present work.

The logarithmic mean temperature difference is

$$\Delta T_m = \frac{\left(T_{s,in} - T_{fg,out}\right) - \left(T_{s,out} - T_{fg,in}\right)}{\ln\left(\frac{T_{s,in} - T_{fg,out}}{T_{s,out} - T_{fg,in}}\right)} \tag{3}$$

The overall heat transfer coefficient is

$$\alpha_{t,exp} = \frac{Q_s}{A_o \Delta T_m} \tag{4}$$

In the above equations, c_p is the specific heat, and A_o is the total heat transfer area based on the outer wall of the heat transfer tubes. Using the error transmission principle, the heat transfer rate and coefficients were estimated to have uncertainties of 1.17% and 9.57%, respectively.

3. Results and discussion

This section consists of two parts: Section 3.1 presents the overall heat transfer coefficients, and Section 3.2 demonstrates the MSHE performance operating in the heat storage and heat compensation modes.

3.1. The overall heat transfer coefficient

To design a flue gas-driven HSS, a calculation method must be developed for the overall heat transfer coefficient, $\alpha_{t,cal}$, which is based on the outer wall surface area of the heat transfer tubes. As $\alpha_{t,cal}$ is inversely proportional to the total thermal resistance $R_{t,cal}$ as in $\alpha_{t,cal} = 1/R_{t,cal}$, we determine $R_{t,cal}$ as [29]

$$R_{t,cal} = \frac{1}{\alpha_s}\frac{d_o}{d_i} + \frac{d_o}{2\lambda}\ln\frac{d_o}{d_i} + \frac{1}{\alpha_{fg}} \tag{5}$$

where the first, second, and third terms on the right side of Eq. (5) represent the thermal resistance of the convection heat transfer of the molten salt, conduction resistance across the tube wall thickness, and thermal resistance of the flue gas, respectively; α_s and α_{fg} are the convective heat transfer coefficients of the molten salt and flue gas, respectively; d_o and d_i are the outer and inner diameters of the heat transfer tubes, respectively; and λ is the thermal conductivity of the tube.

The α_{fg} is calculated as [30]

$$\alpha_{fg} = \left(\frac{A_f}{A}E + \frac{A_s}{A}\right)\frac{0.85\alpha_d}{1 + 0.00425\alpha_d} \tag{6}$$

$$\alpha_d = 0.105\left(\frac{\lambda_{fg}}{S}\right)\left(\frac{d_o}{S}\right)^{-0.54}\left(\frac{h}{S}\right)^{-0.14}\left(\frac{v_f S}{v}\right)^{0.72} \tag{7}$$

where A_f is the contact area between the fins and the flue gas, A is the equivalent surface area based on the outer diameter of the heat transfer tubes, E is the fin efficiency, A_s is the contact area between the heat transfer tubes and the flue gas, λ_{fg} is the thermal conductivity of the flue gas, h is the fin height, v_f is the flue gas velocity, S is the pitch distance between neighboring fins, and v is the dynamic viscosity of the flue gas.

Several experimental studies were conducted on the convection heat transfer of molten salt in circular tubes covering different ranges of Reynolds numbers (Re). To develop a general heat transfer correlation, the data of Hoffman and Cohen [31], Chen et al. [32], Chen et al. [33], Chen et al. [34], Qian et al. [35], and Hu [36] are summarized in Fig. 6(a), which are presented using the vertical and horizontal coordinates $Nu_s/Pr_s^{1/3}$ and Re_s, respectively, where Nu is the Nusselt number, Pr is the Prandtl number, and the subscript s indicates the molten salt. Here, we develop a combined heat transfer correlation covering a wide Re_s range with a smooth transition from a laminar regime to a transition regime, and from a transition regime to a fully developed turbulent regime.

Based on the limited experimental data for laminar flow, we obtained the heat transfer correlation in this regime as:

$$Nu_s = (0.001412Re_s + 6.217)Pr_s^{1/3}, Re_s < 2300 \tag{8}$$

In the transition regime of 10 000 < Re_s < 120 000 and 0.7 < Pr_s < 120, Colburn [37] presented

$$Nu_s = 0.023Re_s^{0.8}Pr_s^{1/3} \tag{9}$$

Wu et al. [38] provided the correlations in the transition and turbulent regimes as follows:

$$\begin{cases} Nu_s = 0.00154Re_s^{1.1}Pr_s^{1/3}, \text{transition regime} \\ Nu_s = 0.0294Re_s^{0.787}Pr_s^{1/3}, \text{turbulent regime} \end{cases} \tag{10}$$

By comparing the experimental data in a narrow transition regime, because of the two correlations of Wu et al. [38] and Colburn [37], one slightly underpredicts and the other overpredicts the heat transfer coefficients, we synthesize the two correlations in this subregime as:

$$Nu_s = 0.5 \times \left(0.00154Re_s^{1.1} + 0.023Re_s^{0.8}\right)Pr_s^{1/3}, 2300 < Re_s < 8200 \tag{11}$$

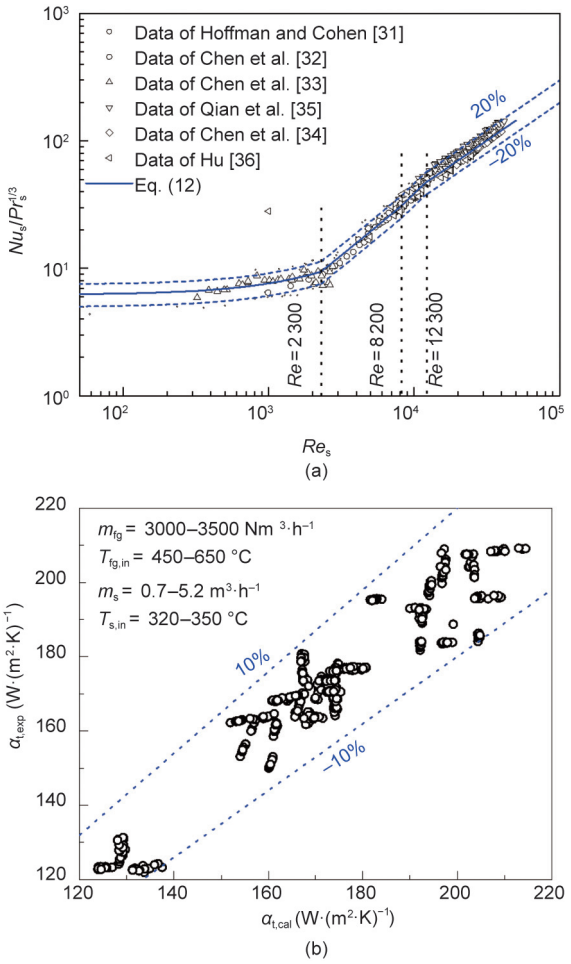

Fig. 6. Heat transfer characteristics. (a) Correlation of Nusselt number versus Reynolds number for molten salt; (b) comparison of measured overall heat transfer coefficients and predicted values.

The above comment yields the correlation over the entire Re_s range as

$$\begin{cases} Nu_s = (0.001412Re_s + 6.217)Pr_s^{1/3}, Re_s < 2300 \text{ (present correlation)} \\ Nu_s = 0.5 \times \left(0.00154Re_s^{1.1} + 0.023Re_s^{0.8}\right)Pr_s^{1/3}, 2300 < Re_s < 8200 \\ \text{(Colburn [37] and Wu et al. [38])} \\ Nu_s = 0.00154Re_s^{1.1}Pr_s^{1/3}, 8\,200 < Re_s < 12\,300 \text{ (Wu et al. [38])} \\ Nu_s = 0.0294Re_s^{0.787}Pr_s^{1/3}, Re_s > 12\,300 \text{ (Wu et al. [38])} \end{cases} \tag{12}$$

The heat transfer coefficient of molten salt is

$$\alpha_s = \frac{\lambda_s Nu_s}{d_i} \tag{13}$$

Substituting Eqs. (6), (7), (12), and (13) into Eq. (5) yields $\alpha_{t,cal}$. Fig. 6(a) compares the predicted $Nu_s/Pr_s^{1/3}$ with the experimental data reported in the literature, demonstrating good accuracy over the entire Re_s range with deviations of less than 20%, which is acceptable for engineering applications. Our experiments cover the following data ranges: flow rate of flue gas $m_{fg,in}$ = 3000–3500 $Nm^3 \cdot h^{-1}$, inlet temperature of flue gas $T_{fg,in}$ = 450–650 °C, flow rate of molten salt m_s = 0.7–5.2 $m^3 \cdot h^{-1}$, and inlet temperature of molten salt $T_{s,in}$ = 320–350 °C, resulting in a wide range of measured overall heat transfer coefficients $\alpha_{t,exp}$. A comparison between $\alpha_{t,cal}$ and $\alpha_{t,exp}$ is shown in Fig. 6(b), which indicates a deviation boundary of

20%. Notably, Fig. 6(a) considers only the convection heat transfer of the molten salt, but Fig. 6(b) considers the overall heat transfer integrating the three resistances from the flue gas to the molten salt. The smaller deviation of Fig. 6(b) than Fig. 6(a) is due to the fact that, even though fins are used to enhance convective heat transfer of flue gas, thermal resistance in the flue gas side is still larger than that in the tube side. Under such circumstances, the overall heat transfer coefficients were insensitive to variations in the convective heat transfer of the molten salt. Our work concluded with a reliable heat transfer calculation for the MSHE, which was verified experimentally.

3.2. Operating in heat storage and compensation modes

The HSS includes heat storage, heat compensation, and salt-receded modes. The heat storage mode pumps salt from the cold tank to the hot tank, absorbing heat via the MSHE (Figs. 7(a)). Stable operation in this mode was achieved for the example shown in Fig. 7(b). The system was successfully controlled by varying the flow rates of the molten salt and flue gas (m_s and m_{fg}) and the two inlet temperatures of the molten salt and flue gas ($T_{s,in}$ and $T_{fg,in}$). The heat transfer rate, also called the heat charging power Q, is plotted against these parameters in Fig. 7(c)–(e). A maximum power of 320 kW was achieved to exceed the 300 kW rated power as the design target. Generally, an increasing trend of Q versus m_s, m_{fg}, and $T_{fg,in}$ is demonstrated, but the slope of these curves becomes gentler when m_s and $T_{fg,in}$ increase, except for m_{fg}. The variation trend shown in Fig. 7 reflects the sensitivity of the controlling parameters to the heat storage rate, providing guidance for an enlarged MSHE design for integration into a coal-fired power plant.

As noted in Section 2, molten salt has been successfully applied in solar thermal plants, where electric heating is used for heat compensation to resist heat release into the environment. In the present study, an innovative strategy is proposed and verified experimentally to reduce electricity consumption using a flue gas heating technique instead of electricity. Fig. 8 shows the principle of the heat compensation mode, in which salt is sucked from the hot tank to the hot tank. For the heat compensation mode, because the temperature difference across the two sides of the MSHE is smaller than that for the heat storage mode, the heat charging rate Q is smaller; for example, at the ~170 kW level (Fig. 8). Notably, steady operation can be achieved for the heat storage mode, but only quasi-steady operation is achieved for the heat compensation mode, because the molten salt temperature in the hot tank increases to decrease the temperature difference between the flue gas and molten salt in the heat exchanger, as evidenced by the increase in $T_{s,in}$ and decrease in Q (Fig. 8).

For the MSHE, attention should be paid to the temperature distribution of the molten salt among the different tube rows. Overheating of salt increases the risk of decomposition. The temperature deviation, defined as the temperature in the branch tubes minus the average value after complete mixing in the common plenum, was set to 10 K, below which no decomposition occurred because the salt did not reach the decomposition temperature. The uniformity of the flow and temperature fields of the flue gas in the tunnel dominated the temperature distribution of salt in the branch tubes. We demonstrate that the temperature deviations are within 4 K for the six rows of tubes, which is below the setting criterion of 10 K for different operating conditions (Fig. 9). The quasi-uniform temperature distribution of the salt was partially due to the two-module design. Cutting the entire heat exchanger into two modules in the height direction, a mixing chamber was added to redistribute the salt in the top section, thereby flattening the temperature distribution when the salt left the heat exchanger.

To further consider the effect of the modular design on the temperature uniformity, the standard deviation of the temperature of the molten salt is expressed as

$$\sigma = \sqrt{\frac{\sum_{i=1}^{n}(T_i - T_{ave})}{n}} \tag{14}$$

where T_i is the temperature of the molten salt at the outlet of the ith row of heat-transfer tubes, n is the total number of rows of heat-transfer tubes (n = 6), and T_{ave} is the average temperature.

Table 1 lists the outcomes based on the measured data provided at the outlets of both modules. Both modules showed standard deviations in the range of (0.85–1.54) °C. By comparing the data between the lower and upper modules, it was concluded that the upper module suppressed the rise in temperature deviation, which was caused by the contribution of the two-module design.

The decreased non-uniformity of salt temperature at the MSHE outlet comes from the intermediate header, also called the common plenum, across the two modules of MSHE. The mixing effect of the salt in the header reduces the transmission of thermal deviation from the bottom module to the top module. As shown in Fig. 10(a), for the six rows of tubes, the maximum deviation from the average value is 4.64 °C at the bottom module outlet, but reduces to 2.74 °C at the top module inlet. Similar phenomenon is also observed in Fig. 10(b). The maximum deviation is 6.21 °C for the bottom module, but decreases to 4.91 °C for the top module.

The transition time depends on the thermal inertia of the HSS. The two running conditions given in Fig. 11 show transition times of 500 and 370 s, respectively. Covering the whole range of running parameters, the transition time is in the range of 180–600 s. The experimentally determined transition time is useful for optimizing heat storage control systems. The switch time from one steady state to a new one depends on the heat transfer from the flue gas to the molten salt, which involves convection heat transfer on the flue gas side and molten salt in the tubes, heat conduction in metallic materials, and the flow time of the molten salt in the tubes. The switch time [39] can be related to metal time constant (τ_m), flow time constant (τ_0), and dynamic constant (a): $\tau_m = G_m c_m/(\alpha_s A_n)$, $\tau_0 = L/w_s$, and $a = \alpha_s A_n/(m_s \rho_s c_{p,s})$, where L is the tube length, A_n is the inner surface area of the metal tubes, ρ_s is the density of the molten salt, w_s is the velocity of the molten salt, G_m is the metal quality of the metal tubes, c_m is the specific heat of the metal tubes. For the running case shown in Fig. 11, the adjustment time was 460–485 s, which matches the measured value of 500 s for the switching time.

The experiments lasted for one year. No weakened flow and heat transfer performances of the MSHE were observed. The three subfigures of Fig. 12 present overall heat transfer coefficients $\alpha_{t,exp}$, distributions of salt temperature T_s, and pressure drops of flue gas ΔP_{fg}.The experimental data shown in Fig. 12 were collected from August 23, 2024 to December 17, 2024. It is seen that the data of overall heat transfer coefficients and pressure drops are overlap with each other on the two different collection durations, demonstrating no obvious variation of flow and heat transfer behaviors on both flue gas side and molten salt side.

4. Applications of the flue gas heat storage technology

China has initiated a project called "super-flexible coal-fired power plant." A major task is to increase the load variation speed of the power plant to 6% Pe·min^{-1}, which is equivalent to that of a gas turbine. To achieve this target, a molten salt system was integrated with a 350 MW coal-fired plant, including a flue gas heat charging subsystem, two tank storage subsystems, and a heat discharging subsystem. The heat charging and discharging subsystems operate at load ratios below 50% turbine heat acceptance

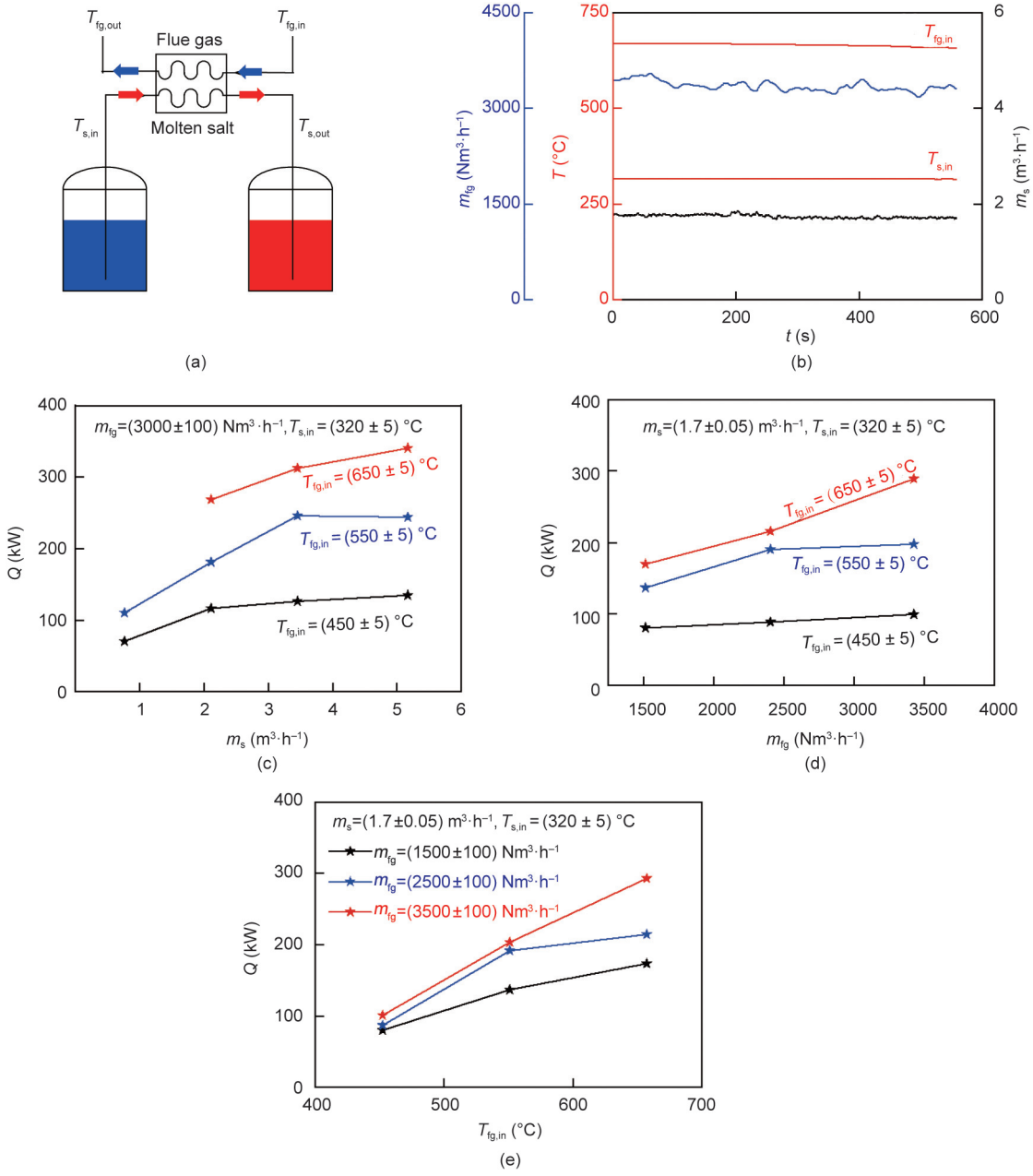

Fig. 7. Steady operation in the heat storage mode. (a) The heat storage mode; (b) parameters versus time on the salt side and flue gas side; (c–e) variation of heat storage rate with various operating parameters.

(THA) and above 50% THA, respectively. The heat charging rate and charging time were 10 MW and 10 h, respectively, which yielded a thermal storage capacity of 100 MW·h. Each heat discharge process involves a triangular distribution of the thermal load with a peak value of 165 MW lasting for a short period of 500 s. Hence, the 100 MW·h storage capacity can sustain seven heat discharge cycles for vapor generation to reach the 6% Pe·min^{-1} target. Our approach belongs to "slow-charging/fast-discharging."

A comparison between flue gas extraction technology and vapor extraction technology is summarized below. Zhu et al. [40] conducted numerical simulations using Ebsilon software, focusing on three schemes: flue gas extraction (Scheme 1), main vapor extraction (Scheme 2), and reheating vapor extraction (Scheme 3). The round-trip efficiency η_h quantifies the economic performance of the HSS. Zhu et al. [40] concluded that η_h reaches 83.5% for the flue gas heat storage scheme, 39.2% for Scheme 2, and 75.3% for Scheme 3, indicating a significant efficiency increase with flue gas extraction technology. For Schemes 2 and 3, only the superheated vapor energy can be transferred to the molten salt, whereas the latent heat and subcooled water energy are transferred to other media, such as secondary air or boiler feed water. In summary, compared to vapor extraction technology, flue gas extraction technology not only offers significantly higher round-trip efficiency but also features a simpler hardware configuration, reducing investment costs.

The flue gas extraction technology and the vapor extraction technology are shown in Fig. 13. For the former, the MSHE is coupled with the boiler flue via a heat storage bypass (Fig. 13(a)). The extraction location and return location of the flue gas are chosen based on the design parameters of the boiler and the MSHE, respectively. The flue gas loop is driven by an independent fan. The extracted flue gas passes through a gas–solid separator to remove ash particles in the flue gas, ensuring clean gas to flush the MSHE. After the flue gas releases its heat to the molten salt,

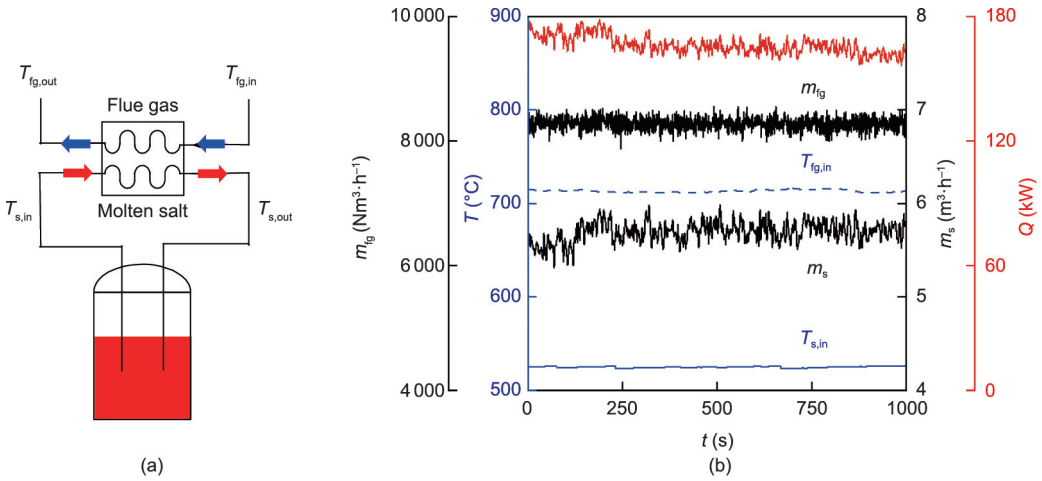

Fig. 8. Quasi-steady operation in the heat compensation mode. (a) Fundamental principle of the heat compensation mode; (b) variations of parameters versus time.

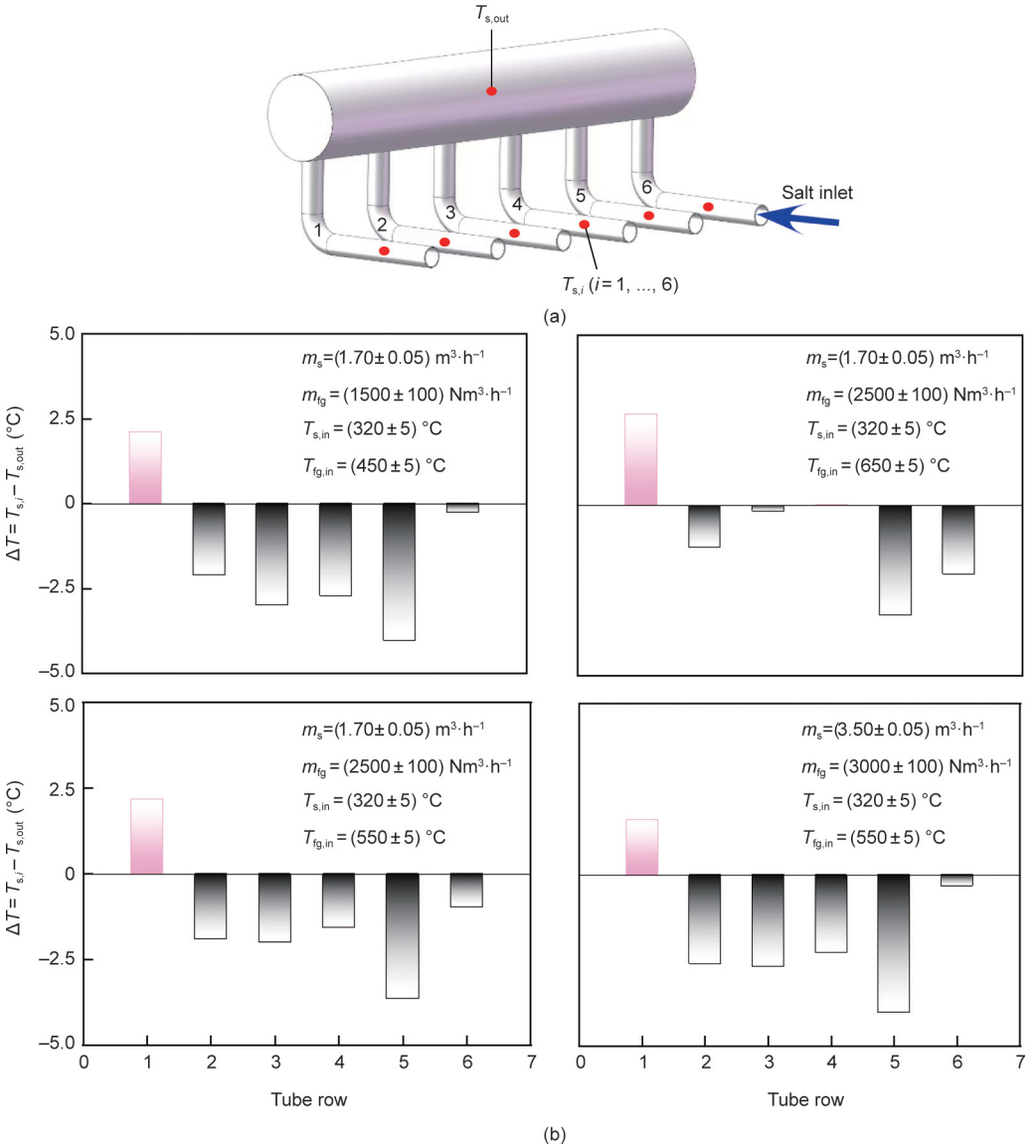

Fig. 9. Thermal deviation of the MSHE under different conditions of flue gas and molten salt. (a) Configuration of the outlet header; (b) thermal deviation of different tube rows.

Table 1
Standard deviation of the molten salt temperatures at the outlets of the two modules.

Module	Standard deviation of temperature (°C; $T_{fg,in}$ = 450 °C)			Standard deviation of temperature (°C; $T_{fg,in}$ = 550 °C)		
	m_{fg} = 1000 $Nm^3 \cdot h^{-1}$	m_{fg} = 2000 $Nm^3 \cdot h^{-1}$	m_{fg} = 3000 $Nm^3 \cdot h^{-1}$	m_{fg} = 1000 $Nm^3 \cdot h^{-1}$	m_{fg} = 2000 $Nm^3 \cdot h^{-1}$	m_{fg} = 1000 $Nm^3 \cdot h^{-1}$
Upper module outlet	1.03	1.00	1.18	1.53	1.54	2.05
Lower module outlet	0.85	0.90	1.13	1.22	1.21	1.25

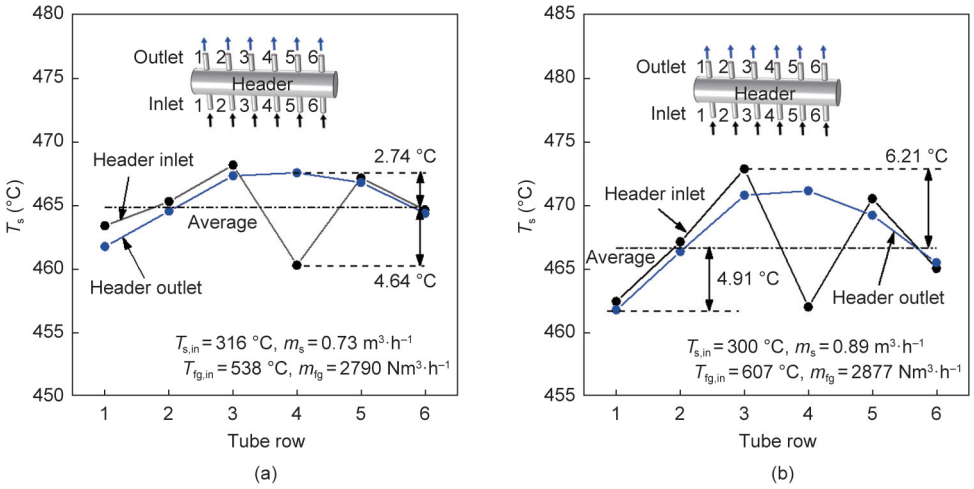

Fig. 10. Comparison of the molten salt temperature distribution at the inlet and outlet of the intermediate header. (a) Molten salt temperature distribution for $T_{fg,in}$ = 538 °C and m_{fg} = 2790 $Nm^3 \cdot h^{-1}$; (b) molten salt temperature distribution for $T_{fg,in}$ = 607 °C and m_{fg} = 2877 $Nm^3 \cdot h^{-1}$.

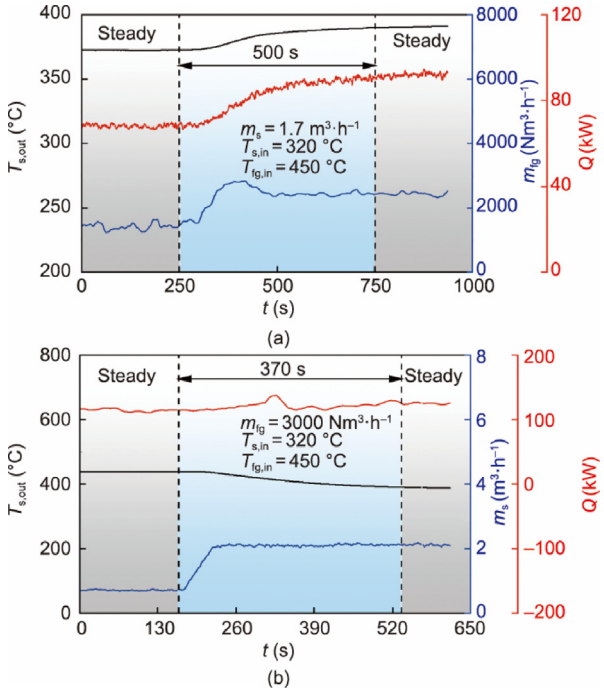

Fig. 11. Transient switch between two steady operating conditions. (a) Transient curves for m_s = 1.7 $m^3 \cdot h^{-1}$, $T_{s,in}$ = 320 °C, and $T_{fg,in}$ = 450 °C; (b) transient curves for m_{fg} = 3000 $Nm^3 \cdot h^{-1}$, $T_{s,in}$ = 320 °C, and $T_{fg,in}$ = 450 °C.

it returns to the SCR inlet of the boiler. The corresponding *T*–*Q* curve does not have TPL (Fig. 13(b)).

For the vapor extraction technology, part of the main vapor is extracted from the power plant to release the heat to a salt heat exchanger, a water heater, and an air heater (Fig. 13(c)). In order to achieve higher salt temperature, the molten salt only receives the superheating sensible heat of vapor. The latent heat and the sensible heat of water are dissipated to the feed water and the secondary air, respectively. The feed water is pumped into the boiler, and the secondary air enters the furnace for combustion, with the corresponding *T*–*Q* curve shown in Fig. 13(d). It is noted that the whole thermal storage system consists of the heat charging side, two tanks of molten salt, and the heat discharging side. Because the heat discharging side is identical for both the flue gas extraction technology and the vapor extraction technology, the discharging side is not discussed here.

Fig. 13 directly illustrates simpler configuration of the flue gas extraction technology than that of the vapor extraction technology. The investment cost is shown in Table 2. For the flue gas extraction technology, major components consist of two salt tanks, a MSHE, a fan, salt pipes and valves, instruments, and so forth. The heat capacity is 10 MW. More components are involved for the vapor extraction technology, including two salt tanks, three heat exchangers, air ducts, pipes, among others. The cost evaluation method for these components is based on Ref. [41]. The outcomes show the total cost of 5.78 million USD for the flue gas extraction technology, and 2.26 million USD for the vapor extraction technology. It is noted that the total heat release of vapor is 11.9 MW, among which only 3.8 MW is stored in the molten salt, the other 8.1 MW is absorbed by the feed water and the secondary air, respectively. Considering the heat storage taking place at 50% THA and the heat discharging stage taking place from 50% THA to 75% THA, the round-trip electricity–electricity efficiency is 68%

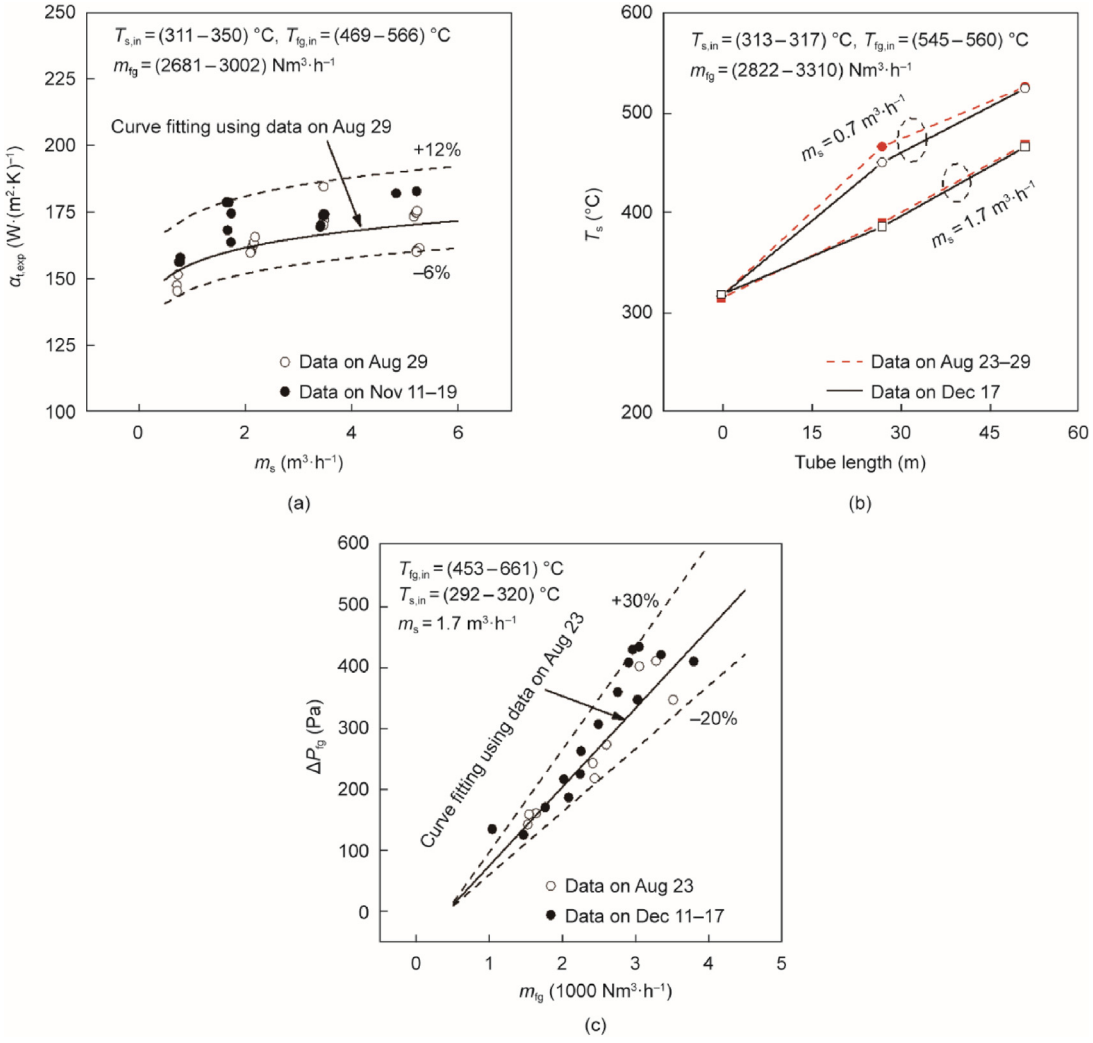

Fig. 12. Performance of the MSHE in long cycle. (a) Weak heat transfer variations for long history operation; (b) salt temperatures collected at different days; (c) weak variations of pressure drops of the MSHE for long history operation.

for the flue gas extraction technology, which is approximately two times of that for the vapor extraction technology.

The return on investment (ROI) of MSHE technology is discussed here. As shown in Table 3, the total capital investment (TCI) is 18.7 million USD for the flue gas driven HSS, including the two tanks and the heat discharging subsystem. The total direct plant cost (TDPC) is approximate 12.6 million USD, with equipment, pipelines and electrical systems, installation, instruments and control, and site construction [18] accounting for 33%, 20%, 25%, 8%, and 14%, respectively.

The ROI depends on China's policy for flexible coal-fired power plant operations. The revenue includes the heat storage part and discharging part, coming from the deep peak regulation and the ramping, respectively. For the heat storage part, considering the 10 MW heat charging rate, a thermal-power conversion efficiency of 40%, a peak regulation depth of 4 MW, continuous peak regulation duration of 10 h, and a peak regulation electricity price of 0.056 USD·(kW·h)$^{-1}$ [18], the annual revenue is 0.82 million USD. For the heat discharging part, considering a ramping power of 87.5 MW, a ramping electricity capacity of 6.08 MW·h, 8 ramping events per day, a compensation standard of 4.3 USD·(MW·d)$^{-1}$ [42] for ramping power and 57 USD·(MW·h)$^{-1}$ for ramping electricity capacity, the annual revenue is 2.11 million USD. Hence, the total revenue is 2.93 million USD for heat charging and discharging processes, yielding six years for cost recovery.

Finally, how the 300 kW experimental outcomes are applied for the design and operation of the 10 MW MSHE is commented here. This design includes heat transfer enhancement using finned tubes, a low inclination angle of heat transfer tubes to prevent salt receding, and a modular design to ensure an even temperature distribution at the heat exchanger outlet. The developed calculation method for the overall heat transfer coefficient supports the design of large-scale heat exchangers. We gained insights from our experimental work to ensure the effectiveness of heat storage and heat compensation that minimizes heat release to the environment in large-scale systems.

In the scaling-up process, the challenges and solutions of flue gas extraction technology are outlined. Because solid particles are entrained in the flue gas stream, a wearing effect may appear owing to the collisions of the particles on the heat transfer tubes, decreasing the lifetime of the heat storage device. Upstream of the MSHE, a gas–solid separator was installed to separate the solid particles from the flue gas stream. Even though a separator is adopted, some fine particles, such as those below 10 μm, still have the possibility to be deposited on the heat transfer tubes, forming ash-particle layers that deteriorate the heat transfer performance. To overcome this shortcoming, flue gas tunnels have been designed to be vertical or inclined. A horizontal flue gas tunnel is avoided. Hence, fine particles settled at the bottom of the tunnel owing to gravity. This design decreased ash layer formation in the heat

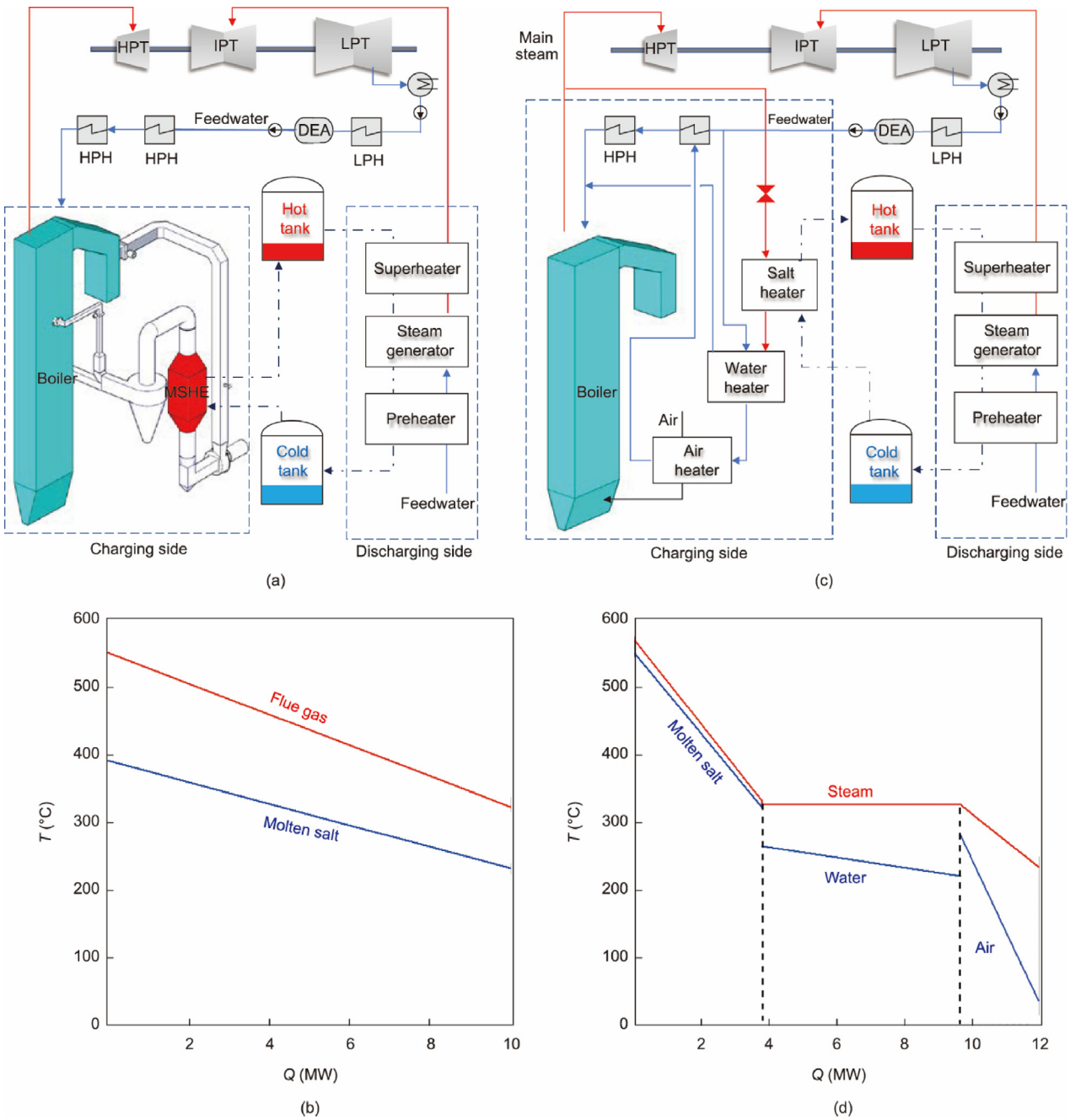

Fig. 13. Comparison of the flue gas extraction technology with the vapor extraction technology. (a) Flow chart of the flue gas-driven heat storage system; (b) *T*–*Q* curve of the flue gas-driven heat transfer; (c) flow chart of the vapor driven heat storage system; (d) *T*–*Q* curve of the vapor driven heat transfer. HPH: high pressure heater; LPH: low pressure heater; DEA: deaerator; HPT: high pressure turbine; IPT: intermediate pressure turbine; LPT: low pressure turbine.

transfer tubes. In addition to the aforementioned hardware, a group of sonic soot blowers was used. After two weeks of operation, the sonic soot blowers cleared fine particles from the heat-transfer tubes. The ash-cleaning technique was successfully applied in our 300 kW MSHE test loop. After one year of operation, no obvious decay in MSHE performance was observed. Such techniques are included in large-scale flue gas heat storage engineering.

Next, we consider the solidification and decomposition of the molten salt. To prevent solidification, the molten-salt pump was not triggered until the MSHE was warmed by the flue gas to a temperature higher than that of the molten salt. To prevent decomposition, two flue gas streams are mixed before entering the MSHE: one with a higher temperature of approximately 550 °C and another with a lower temperature of approximately 300 °C. If the temperature or flow rate of the higher-temperature stream increases, posing a risk of salt decomposition, the flow rate of the lower-temperature stream is increased. Mixing the two streams of flue gas ensured a conformable temperature at the MSHE inlet to prevent decomposition of the molten salt. In summary, the dual-stream technique increases the degree of flexibility of the HSS.

The materials and operating temperatures of the MSHE influence the corrosion rate of the HSS. TP347H, which has been commercially used in coal-fired and solar thermal power plants [43,44], can withstand high temperatures up to 700 °C. Therefore, it is selected as the base material for fabricating the MSHE. In current applications, the operating temperature of the MSHE is more

Table 2
Investment comparison between flue gas and steam extraction thermal storage technologies.

No.	Flue gas extraction method		Vapor extraction method	
	Equipment	Estimated cost (USD)	Equipment	Estimated cost (USD)
1	Salt tanks	564 726	Salt tanks	564 726
2	MSHE	2 611 383	Salt heater	183 219
3	Flue duct and dampers	804 805	Water heater	109 067
4	Fan	373 000	Air heater	246 932
5	Salt pumps	548 625	Salt pumps	548 625
6	Salt pipe and valves	490 254	Air duct and dampers	201 201
7	Instruments	392 203	Salt pipes and valves	185 377
8	—	—	Water pipes and valves	128 904
9	—	—	Instrument	88 466
10	Total	5 784 996	Total	2 256 517

The investment of the heat discharging side are not included in this table.

Table 3
Total investment of the flue gas driven thermal storage system.

Item	Cost (USD)
Total capital investment (TCI)	18 681 581
Total direct plant costs (TDPC)	12 609 400
Indirect costs (14% TDPC)	1 765 315
Contingencies and owner's costs (17% TDPC)	2 156 207
Total fixed O&M cost (4.8% TCI)	896 716
Total variable O&M cost (salt cost)	1 253 943

O&M: operation and maintenance.

than 100 °C lower than the temperature endurance limit of the material, thereby reducing the corrosion risk. The flue gas and molten salt are separated by the tube wall. The flue gas may not be in contact with the molten salt. The corrosion of flue gas on the tube walls can be neglected owing to the "dry" flue gas at the temperature level of ~500 °C. In a thermal power plant, corrosion only occurs at the "wet" condition when the flue gas temperature approaches the acid dew point at ~100 °C level [45]. The pressure drop and heat transfer coefficient of the MSHE do not change significantly after one year of operation, which can be attributed to the presence of weak corrosion in our developed system.

5. Conclusions

We successfully demonstrated the concept design, fabrication, and testing of a flue gas-driven HSS. The challenges of the MSHE are presented. Innovative strategies have been proposed to overcome these challenges, including finned tubes to enhance the convective heat transfer of flue gas, weak inclination angles for heat transfer tubes, and modular designs. A hybrid heat transfer correlation of molten salt was presented, covering a wide range of Reynolds numbers from the laminar regime to the turbulent regime, which was verified to have a maximum uncertainty of 20% by comparison with experimental data in the open literature. A calculation method for the overall heat transfer coefficient was proposed and verified to deviate from our present experiment by less than 10%. Our developed system is believed to have heat storage and heat compensation functions to resist the release of heat into the environment. The temperature differences were found to be less than 4 K among the various tube rows, ensuring no decomposition of the molten salt during the operation. Switching from one steady state to another steady state is tested to have the transition time within 180–600 s. We conclude that the outcomes obtained in this study are important for supporting large-scale MSHE design and operation, and assisting coal-fired power plants in increasing flexibility.

Various energy storage technologies have been developed to compensate for the instability of renewable energy sources. Flue gas heat storage technology can be regarded as a new family of energy storage schemes that can overcome the limitations of the vapor extraction technology. Challenges such as matching thermal resistance, cleaning ash deposition, preventing solidification, and preventing the decomposition of molten salt have been addressed through experiments. Our work can be extended to other fields, such as metallurgy and the chemical industry, where flue gases are abundant, to save or store energy.

CRediT authorship contribution statement

Jinliang Xu: Writing – review & editing, Validation, Methodology, Investigation, Data curation, Conceptualization. **Hongliang Su:** Writing – original draft, Methodology, Investigation, Formal analysis, Data curation, Conceptualization. **Xinyu Dong:** Writing – original draft, Validation, Methodology, Investigation, Formal analysis, Data curation. **Xiongjiang Yu:** Writing – review & editing, Supervision, Methodology, Conceptualization. **Chao Liu:** Writing – review & editing, Supervision, Methodology, Conceptualization. **Yan Wang:** Methodology, Formal analysis. **Jian Xie:** Methodology, Formal analysis. **Wei Wang:** Supervision, Project administration. **Yupu Yu:** Methodology, Formal analysis. **Qinghua Wang:** Supervision, Conceptualization. **Yuguang Niu:** Supervision, Conceptualization. **Jizhen Liu:** Supervision, Conceptualization. **Ying Huang:** Supervision, Conceptualization. **Zhengshun Zhang:** Supervision, Conceptualization. **Anyou Dong:** Supervision, Conceptualization. **Yan Pan:** Supervision, Project administration. **Hao Wu:** Supervision, Project administration.

Declaration of competing interest

The authors declare that they have no known competing financial interests or personal relationships that could have appeared to influence the work reported in this paper.

Acknowledgments

The authors thank for the financial support by the Coal-Major Project (2024ZD1700300) and the National Natural Science Foundation of China (52406183).

References

[1] Li J, Khan I. Transition to a sustainable energy balance and conversion factors in economic management: basics for transitioning to a low-carbon economy. Energy 2024;313:133724.
[2] Paraschiv LS, Paraschiv S. Contribution of renewable energy (hydro, wind, solar and biomass) to decarbonization and transformation of the electricity generation sector for sustainable development. Energy Rep 2023;9:535–44.
[3] Zahid H, Zulfiqar A, Adnan M, Iqbal S, Mohamed SEG. A review on socio-technical transition pathway to European super smart grid: trends, challenges and way forward via enabling technologies. Results Eng 2025;25:104155.

[4] Butt OM, Zulqarnain M, Butt TM. Recent advancement in smart grid technology: future prospects in the electrical power network. Ain Shams Eng J 2021;12(1):687–95.
[5] Li M, Li F, Qiu J, Zhou H, Wang H, Lu H, et al. Multi-objective optimization of non-fossil energy structure in China towards the carbon peaking and carbon neutrality goals. Energy 2024;312:133643.
[6] Henderson C. Increasing the flexibility of coal-fired power plants. Report. London: International Energy Agency; 2014.
[7] Laugs GAH, Benders RMJ, Moll HC. Balancing responsibilities: effects of growth of variable renewable energy, storage, and undue grid interaction. Energy Policy 2020;139:111203.
[8] Wang Z, Liu M, Yan H, Zhao Y, Yan J. Improving flexibility of thermal power plant through control strategy optimization based on orderly utilization of energy storage. Appl Therm Eng 2024;240:122231.
[9] Gonzalez-Salazar MA, Kirsten T, Prchlik L. Review of the operational flexibility and emissions of gas- and coal-fired power plants in a future with growing renewables. Renew Sustain Energy Rev 2018;82:1497–513.
[10] Xu J, Zhang Q, Ye N, Zhang Z, Wu X, Fan H. A review on flexible peak shaving development of coal-fired boilers in China under the carbon peak and carbon neutrality goals. Therm Sci Eng Prog 2024;55:103004.
[11] Arévalo P, Ochoa-Correa D, Villa-Ávila E. Advances in thermal energy storage systems for renewable energy: a review of recent developments. Processes 2024;12(9):1844.
[12] Wang D, Liu D, Wang C, Zhou Y, Li X, Yang M. Flexibility improvement method of coal-fired thermal power plant based on the multi-scale utilization of steam turbine energy storage. Energy 2022;239:122301.
[13] Pescia D. Flexibility in thermal power plants. Report. Berlin: Agora Energiewende; 2017.
[14] Eslick JC, Zamarripa MA, Ma J, Wang M, Bhattacharya I, Rychener B, et al. Predictive modeling of a subcritical pulverized-coal power plant for optimization: parameter estimation, validation, and application. Appl Energy 2022;319:119226.
[15] Taler J, Trojan M, Taler D, Dzierwa P, Kaczmarski K. Improving flexibility characteristics of 200 MW unit. Arch Thermodyn 2017;38(1):75–90.
[16] Richter M, Oeljeklaus G, Görner K. Improving the load flexibility of coal-fired power plants by the integration of a thermal energy storage. Appl Energy 2019;236:607–21.
[17] Liu M, Steven Tay NH, Bell S, Belusko M, Jacob R, Will G, et al. Review on concentrating solar power plants and new developments in high temperature thermal energy storage technologies. Renew Sustain Energy Rev 2016;53:1411–32.
[18] Ma T, Li Z, Lv K, Chang D, Hu W, Zou Y. Design and performance analysis of deep peak shaving scheme for thermal power units based on high-temperature molten salt heat storage system. Energy 2024;288:129557.
[19] Pan L, Shi W. Investigation on the pinch point position in heat exchangers. J Therm Sci 2016;25(3):258–65.
[20] Li Z, Zhang Q, Wang Z, Li J, Ruan Y. Numerical and experimental study of solidification dangers in a molten salt receiver for cloudy conditions. Sol Energy 2019;193:118–31.
[21] Maccari A, Bissi D, Casubolo G, Guerrini F, Lucatello L, Luna G, et al. Archimede solar energy molten salt parabolic trough demo plant: a step ahead towards the new frontiers of CSP. Energy Procedia 2015;69:1643–51.
[22] Rodríguez-García MM, Herrador-Moreno M, Moya EZ. Lessons learnt during the design, construction and start-up phase of a molten salt testing facility. Appl Therm Eng 2014;62(2):520–8.
[23] Bonanos AM, Georgiou MC, Stokos KG, Papanicolas CN. Engineering aspects and thermal performance of molten salt transfer lines in solar power applications. Appl Therm Eng 2019;154:294–301.
[24] González-Roubaud E, Pérez-Osorio D, Prieto C. Review of commercial thermal energy storage in concentrated solar power plants: steam vs molten salts. Renew Sustain Energy Rev 2017;80:133–48.
[25] Serrano-López R, Fradera J, Cuesta-López S. Molten salts database for energy applications. Chem Eng Process 2013;73:87–102.
[26] Zhou J, Xie X, Tang S, Xu Y, Li X. Numerical investigation and comparison on thermal–hydraulic performance of H-type finned tube heat exchanger. Case Stud Therm Eng 2024;59:104481.
[27] Xu J, Gan Y, Zhang D, Li X. Microscale heat transfer enhancement using thermal boundary layer redeveloping concept. Int J Heat Mass Transf 2005;48(9):1662–74.
[28] Chaves J, Lasanta MI, García-Martín G, De Miguel MT, Pérez FJ. Degradation mechanism of AISI 316L, 321H, and 347H alloys in ternary molten salt vs solar salt. Results Eng 2025;25:104051.
[29] Kothandaraman CP. Fundamentals of heat and mass transfer. 3rd ed. Daryaganj: New Age International; 2006.
[30] Lin Z, Xu T. Utility boiler handbook. 3rd ed. Beijing: Chemical Industry Press; 2022. Chinese.
[31] Hoffman HW, Cohen SI. Fused salt heat transfer—Part III: forced-convection heat transfer in circular tubes containing the salt mixture $NaNO_2$–$NaNO_3$–KNO_3. Report. Oak Ridge: Oak Ridge National Laboratory; 1960.
[32] Chen Y, Zhu H, Tian J, Fu Y, Tang Z, Wang N. Convective heat transfer characteristics in the laminar and transition region of molten salt in concentric tube. Appl Therm Eng 2017;117:682–8.
[33] Chen Y, Tian J, Sun S, Sun Q, Fu Y, Tang Z, et al. Characteristics of the laminar convective heat transfer of molten salt in concentric tube. Appl Therm Eng 2017;125:995–1001.
[34] Chen Y, Wang Y, Zhang J, Yuan X, Tian J, Tang Z, et al. Convective heat transfer characteristics in the turbulent region of molten salt in concentric tube. Appl Therm Eng 2016;98:213–9.
[35] Qian J, Kong Q, Zhang H, Zhu Z, Huang W, Li W. Experimental study for shell-and-tube molten salt heat exchangers. Appl Therm Eng 2017;124:616–23.
[36] Hu Q. Experimental study of forced convective heat transfer with mixed nitrate molten slats in a circular tube and corrosion of mixed carbonate molten salts [dissertation]. Beijing: Beijing University of Technology; 2010. Chinese.
[37] Colburn AP. A method of correlating forced convection heat-transfer data and a comparison with fluid friction. Int J Heat Mass Transf 1964;7(12):1359–84.
[38] Wu Y, Chen C, Liu B, Ma C. Investigation on forced convective heat transfer of molten salts in circular tubes. Int Commun Heat Mass Transf 2012;39(10):1550–5.
[39] Shi X, Wang M, Chen C, Lu Z. Technical manual for thermal power generation equipment. Beijing: China Machine Press; 2002. Chinese.
[40] Zhu C, Zhang G, Zhu K, Xu J, Niu Y, Liu J. A molten salt energy storage integrated with combined heat and power system: scheme design and performance analysis. Energy 2024;313:133755.
[41] Seider W, Lewin D, Seader J, Widagdo S, Gani R, Ka M. Product and process design principles: synthesis, analysis and evaluation. 4th ed. Hoboken: John Wiley; 2010.
[42] Trading rules for Guizhou electric power ramping ancillary service market. Report. Guizhou: Guizhou Energy Regulatory Office of National Energy Administration of China; 2024.
[43] Barnard P. Austenitic steel grades for boilers in ultra-supercritical power plants. In: Di Gianfrancesco A, editor. Materials for ultra-supercritical and advanced ultra-supercritical power plants. Cambridge: Woodhead Publishing; 2017. p. 99–119.
[44] Xiao J, Ren J, Xiao S, Zhang H, Chen J, Ren Y, et al. Corrosion behavior of different alloys in novel chloride molten salts for concentrating solar power plants. Sol Energy Mater Sol Cells 2025;286:113531.
[45] Li M, Tang S, Wang F, Zhao Q, Tao W. Gas-side fouling, erosion and corrosion of heat exchangers for middle/low temperature waste heat utilization: a review on simulation and experiment. Appl Therm Eng 2017;126:737–61.